Title: In Situ Conversion of Porphyrin Microbubbles to Nanoparticles for Multimodality Imaging

Authors: Elizabeth Huynh[1,2], Ben Y. C. Leung[3], Brandon L. Helfield[2,3], Mojdeh Shakiba[1,2], Julie-Anne Gandier[5], Cheng S. Jin[1,4,6], Emma R. Master[5], Brian C. Wilson[1,2], David E. Goertz[2,3] and Gang Zheng*[1,2,4,6]

[1]*Princess Margaret Cancer Center and Techna Institute, University Health Network, Toronto, Ontario M5G1L7, Canada.*
[2]*Department of Medical Biophysics, University of Toronto, Ontario M5G1L7, Canada.*
[3]*Sunnybrook Health Sciences Center, Toronto, Ontario M5S 1A1, Canada.*
[4]*Department of Pharmaceutical Sciences, University of Toronto, Ontario M5G1L7, Canada.*
[5]*Department of Chemical Engineering and Applied Chemistry, University of Toronto, Ontario, M5G1L7, Canada.*
[6]*Institute of Biomaterials and Biomedical Engineering, University of Toronto, Ontario, M5G1L7, Canada.*

*Corresponding author: gzheng@uhnresearch.ca

Text:

Converting nanoparticles or monomeric compounds into larger supramolecular structures by endogenous[1, 2] or external[3, 4] stimuli is increasingly popular because these materials are useful for imaging and treating diseases. However, conversion of microstructures to nanostructures is less common. Here we show the conversion of microbubbles to nanoparticles using low frequency ultrasound. The microbubble consists of a bacteriochlorophyll-lipid shell around a perfluoropropane gas. The encapsulated gas gives ultrasound imaging contrast and the porphyrins in the shell confer photoacoustic and fluorescent properties. Upon exposure to ultrasound, the microbubbles burst and formed smaller nanoparticles that possess the same optical properties as the original microbubble. We show this conversion is possible in tumour bearing mice, and could be validated using photoacoustic imaging. Through this conversion, our microbubble can potentially be used to bypass the enhanced permeability and retention effect when delivering drugs to tumours.

The intrinsic conversion of supramolecular structures involves the activation of shape transitions. Of growing interest in the biomedical field, is the conversion of perfluorocarbon nanodroplets as activatable US contrast agents. These nanometre-sized droplets expand to form micron-sized bubbles upon heating[5, 6]. Despite a growing number of investigations utilizing the conversion from nano-to-micron sized structures, to our knowledge, there have not been any studies exploiting the advantages of a micro-to-nano conversion. The most conventional micron-sized structure investigated for biomedical applications is the microbubble, a gas-filled microsphere formed with a biocompatible shell composed of lipids, proteins or polymers. In addition to being US contrast agents, microbubbles have also been studied for their bursting behaviour in response to destructive US for the measurement of blood flow parameters[7] and drug and gene delivery[8]. Interaction of a lipid microbubble with US pulses of sufficient amplitude can

result in its fragmentation or shrinkage, which may be accompanied by the 'shedding' of shell material[9]. These processes lead to the formation of structures that have significantly decreased US imaging contrast relative to the initial microbubble[10]. Furthermore, the remnants of the microbubbles, the lipids themselves, do not serve any imaging purpose.

Recently, we discussed the concept of intrinsically multimodal contrast agents[11] and developed multimodal US contrast agents, in which the building blocks of the microbubble had optical and metal chelation properties. We used a porphyrin-lipid to form a shell around a perfluorocarbon gas forming porphyrin microbubbles (pMBs). The encapsulated gas provided US imaging contrast and the high density of porphyrins enabled photoacoustic and fluorescence contrast[12, 13]. Here we utilize these properties to investigate the response of pMBs to low frequency US. The unique characteristic of forming the multimodality microbubble with building blocks that possess intrinsic optical properties ensures that the responses observed are properties of the pMB after destruction and forming porphyrin nanoparticles (pNPs) from the pMB (Fig. 1a,b), and not simply the release of imaging agents from the microbubble as others have investigated[14].

While previously reported pMBs were formed using pyropheophorbide-lipid, the current pMBs were formed using a bacteriochlorophyll-lipid (BChl-lipid) (Fig.1a), which possessed more favourable optical properties in the near-infrared window. pMBs had a final concentration of $(8.4\pm0.4)\times10^7$ MB/ml and were acoustically responsive with a resonance attenuation peak at 4.5MHz (Fig.2a). pMBs were able to generate both a linear and non-linear responses to US. A tissue mimicking flow phantom containing a wall-less vessel was imaged with a clinical US scanner, and filled with saline or pMBs. The phantom produced linear backscatter shown in the B-mode image, similar to tissue, but did not possess non-linear properties. When pMBs filled the vessel, they were able to produce both linear backscatter and non-linear responses (Fig.2b). The pMB peak size distribution was between 2-8μm by volume (Fig.2c) with 99.9% <10μm by number (Supplementary Fig.1). After activation, pMBs were stable in solution for 1hr after opening the sample vial, after which the pMB concentration decreased to <80% of its initial concentration (Supplementary Fig.2). pMBs were used immediately after opening the vial or within 30min. pMBs had an *in vivo* circulation time of ~2min (Supplementary Fig.3), determined by US imaging, similar to other coated microbubbles[15].

pMB samples were exposed to 1MHz, high duty cycle (50%) US ($2W/cm^2$), hereafter referred to as conversion US, in 2s pulses and were characterized after sonication with 0, 1, 3 or 10 pulses. A decrease in the overall pMB population volume and concentration was observed even after 1 pulse of conversion US; further decrease was observed by increasing the number of pulses (Fig.2c; Supplementary Fig.1 and 4). After 10 pulses, the majority of the pMBs had undergone conversion. The pMB concentration decreased as the pNP concentration increased after each conversion US pulse (Fig.2d).

Furthermore, the resulting pNPs were polydisperse in size between 5–500nm in which 99% of pNPs in all samples were <500nm (Fig.2e, Supplementary Fig.5). Although there were some residual pNPs present without any US pulses applied due to the washing and nanoparticle isolation procedures, an increase in pNP concentration was observed after applying conversion US pulses. pNPs were stable in solution for at least 3 weeks (Supplementary Fig.6).

Light microscopy confirmed the formation of spherical micron-sized pMBs (Fig.2f), which became spherical nanoparticles after interaction with conversion US, seen by electron microscopy (Fig.2g). The majority of the resulting pNPs formed after conversion appeared to be similar in morphology (Supplementary Fig.7). Applying a greater number of conversion US pulses (e.g. 20) did not further induce any changes in morphology in the pNPs (Supplementary Fig.8). We hypothesized that the porphyrin-lipid shell and perfluorocarbon comprising the pMBs were the components forming the pNPs after conversion with US. To investigate the contents of the nanostructure, pMBs were converted into pNPs and then were introduced into vacuum conditions. Electron microscopy revealed that the resulting nanostructures from the pNP samples, after exposure to vacuum conditions, had generated liposome-like bilayer vesicles (Fig.2h), indicating that after conversion from pMBs, the pNPs contained perfluorocarbons from pMBs. Flow field-flow fractionation revealed that BChl-lipid was distributed across pNPs of different sizes (Supplementary Fig.9).

While the specific mechanism of conversion of pMBs to pNPs remains to be investigated, the increased number density of pNPs relative to pMBs is consistent with the occurrence of pMB fragmentation. As noted earlier, the fragmentation and lipid shedding response of encapsulated microbubbles has been previously investigated, however, these studies have been conducted in the context of individual optical microbubble experiments[16, 17] and has not reported the response of a population of microbubbles. Therefore, to investigate whether this micro-to-nano conversion was specific to pMBs, “regular” microbubbles were generated in the same manner as pMBs, except with the substitution of porphyrin-lipid with 1,2-dipalmitoyl-sn-glycero-3-phosphocholine, a phospholipid without a porphyrin group attached. After sonication with conversion US, these regular microbubbles also formed nanostructures similar to the pNPs (Supplementary Fig.10). However, these nanostructures do not possess any additional imaging or therapeutic functionality due to the absence of the porphyrin component.

We investigated the effects of the conversion from microbubble to nanoparticle on the optical properties of pMBs. pMBs exhibited a peak absorbance at 824nm, which is red-shifted from the 750nm absorption peak characteristic of monomeric BChl (Fig.3a). This 74nm bathochromic shift and increase in intensity are signature characteristics of ordered aggregation (J-aggregation)[18] of the porphyrins in the monolayer shell. The presence of ordered aggregates in pMBs was confirmed using circular dichroism spectroscopy, which displayed peaks corresponding to the absorption spectra of pMBs and was void of

peaks with the BChl monomeric sample in which the aggregates had been disrupted (Fig.3b). Upon application of conversion US pulses, the background scattering decreased, correlating to a decrease in microbubble concentration, yet the peak absorbance and ordered aggregates at 824nm was maintained (Fig.3a,b). This behaviour was also confirmed in serum, ensuring the optical functionality of this conversion in the presence of serum proteins (Supplementary Fig.11). The 824nm peak absorbance of the pNPs was maintained even when incubated in serum, gradually decreasing over time to 75% of the initial absorbance after 3hr (Supplementary Fig.12). This was observed with an increase in the monomeric 750nm peak absorbance, indicating a disruption of the ordered aggregates.

Photoacoustic imaging is an emerging technique that combines advantages of both US and optical imaging and is based on the absorption of light, thermoelastic expansion and detection of the generated US waves[19]. The photoacoustic spectra of pMBs before and after sonication corresponded well with the absorption spectra, maintaining a peak signal at 824nm (Fig.3c). Furthermore, pMBs were also able to generate fluorescence as a result of their ordered aggregation, with an emission peak at 830nm, red shifted from the BChl monomeric fluorescence emission peak at 765nm (Supplementary Fig.13). The ordered aggregation peak at 830nm was also maintained even with the conversion to pNPs (Fig.3d). An increase in fluorescence emission was observed after application of conversion US. This has been previously observed with other groups, and was attributed to scattering of the excitation and emission light by the gas[20].

To demonstrate the imaging capabilities of pMBs and pNPs, samples were embedded in a polyacrylamide gel and imaged using US, photoacoustic and fluorescence. US imaging showed a distinct decrease in contrast with a greater number of conversion US pulses applied (Fig.4a), which was further verified with a relative comparison in contrast mean power between samples (Fig.4b). The photoacoustic and fluorescence intensities remained consistent in pMBs and pNPs after conversion and were not statistically significant ($p>0.05$) between pulsed samples (Fig.4a,c,d). Differences observed in fluorescence intensity between the phantom imaging and spectra in Figure 3d may be due to detector sensitivity, as the detector used to obtain the fluorescence spectra is more sensitive than the camera used for imaging. These phantom images confirm the applicability of trimodal imaging of pMBs, applying the unique US property of microbubbles, their ability to burst, shrink or fragment in response to US, and optically image the resulting nanoparticles formed.

Porphyrin-based nanoparticles have been of increasing interest for imaging and treatment of disease, in particular, cancer, due to their intrinsically multifunctional nature. They have been applied as fluorescence imaging[21], positron emission tomography[22, 23], magnetic resonance imaging[24] and photoacoustic imaging[21, 25] contrast agents, as well as for photodynamic therapy (PDT)[26] and photothermal therapy (PTT)[27]. As with the majority of nanoparticles intended for tumour targeting, the

delivery of these porphyrin-based nanoparticles relies on the enhanced permeability and retention (EPR) effect, requiring on the order of hours to days for maximum accumulation. However, the clinical relevance of the EPR effect has undergone significant debate due to difficulty in predicting nanoparticle uptake *in vivo* as a result of a number of factors affecting EPR, such as heterogeneity in the vascular bed, tumour growth microenvironment and infiltrating macrophages. Furthermore, the EPR effect has also not been well understood and correlated between preclinical and clinical patient solid tumours[28]. Alternatively, microbubbles have been investigated for drug and gene delivery, in which a drug-loaded microbubble may interact with US causing the microbubble to burst and form non-lethal transient pores in blood vessels through which drugs may extravasate[8]. Therefore, we sought to utilize the micro-to-nano conversion of pMBs to bypass the EPR effect, using an external trigger, to deliver pNPs to a solid tumour.

pMBs were intravenously injected into KB xenograft bearing mice and the mice were divided into two groups in which the tumour was either subjected to conversion US ("conversion US applied" group) or did not have conversion US applied ("no conversion US applied" group). US imaging was used to monitor the influx of pMBs into the tumour (Fig.5a,b). When conversion US was not applied, the pMBs circulated for approximately 2min before returning to baseline (Fig.5a,b). In contrast, in the conversion US applied group, after 20s post injection, in which the pMBs could be observed circulating in the tumour, conversion US was applied and a decrease in US contrast was observed within a few seconds, quickly returning back to baseline (Fig.5a,b), indicating conversion from pMB to pNP.

Photoacoustic imaging was used to verify the conversion to pNP and validate successful delivery and retention of porphyrins in the tumour. When conversion US sonicated the tumour after injection of pMBs, the photoacoustic signal was maintained within the tumour for at least 2hrs. However, when conversion US was not applied, the photoacoustic signal decreased within 30min post-injection. (Fig.5c,d). Fluorescence imaging of whole blood was used to investigate the cause of this decrease in photoacoustic signal. The US contrast from pMBs is generated from the presence of gas within the microbubble. After 2min of circulation, this gas diffuses out of the pMB, however, the lipid shell may still form some remnant structure, which remains in circulation and will also be cleared by the reticuloendothelial system. Fluorescence imaging of whole blood extracted after pMB injection revealed that after 5min of circulation, the ordered aggregation peak remained intact with the fluorescence emission peak at 830nm. However, by 30min, the ordered aggregation had been disrupted, shifting back to its monomeric fluorescence emission peak at 765nm (Supplementary Fig.14). This corresponded to the observed decrease in photoacoustic signal without application of conversion US. Therefore, the presence of photoacoustic signal in tumours with conversion US indicates the successful delivery of porphyrins, in the structure of pNPs, to the tumour. Thus, we envision the use of photoacoustic or another imaging

modality to confirm successful delivery of pNPs via the *in situ* conversion within minutes of administration, which can then be used for therapy (e.g. PDT or PTT).

pMBs are trimodality contrast agents for US, photoacoustic and fluorescence. Furthermore, they also respond to low frequency US, forming nanoparticles. Other studies have generated nanoparticle-microbubble composites to deliver nanoparticles such as gold[29]. However, pMBs are unique in that the nanoparticle is generated from the microbubble instead of using an encapsulation or tethering approach. Furthermore, porphyrins also have a self-delivery function[30], and thus, once across the vasculature, the pNPs can enter into tumour cells. The presence of the porphyrin in pMBs has transformed a conventional microbubble from a unimodal US contrast agent and delivery vehicle, without any function after bursting, to a trimodality contrast agent in which the resultant nanoparticle has imaging and therapeutic properties and can be delivered to tumours without relying on the EPR effect. Therefore, pMBs introduce a plethora of new imaging and therapeutic applications for microbubbles, harnessing the advantages of US-based methods.

Materials and Methods:

pMB and pNP fabrication and size characterization

To form pMBs, a 1mg lipid mixture consisting of 40mol% porphyrin-lipid (bacteriochlorophyll (BChl)-lipid as previously described[21]), 42mol% 1,2-dipalmitoyl-sn-glycero-3-phosphocholine (DPPC), 10mol% 1,2-dipalmitoyl-sn-glycero-3-phosphate (DPPA) and 8mol% 1,2-dipalmitoyl-sn-glycero-3-phosphoethanolamine-N-[methoxy(polyethylene glycol)-5000] (DPPE-mPEG5000) were combined in chloroform in 12mm x 35mm glass threaded vials (Fisher Scientific). For experiments using regular microbubbles without porphyrin-lipid, the porphyrin-lipid in the mentioned formulation was replaced with DPPC. DPPC, DPPA and DPPE-mPEG5000 lipids were purchased from Avanti Polar Lipids Inc. (Alabaster, AL). The chloroform was dried by nitrogen gas and vacuumed for 1hr to form a lipid film. Lipid films were then rehydrated with 1ml of 10vol% glycerol, 10vol% propylene glycol and 80vol% phosphate buffered saline (PBS). Sample vials were topped off with perfluoropropane gas (C_3F_8, PFP, Fluoromed L.P), briefly heated with a heated water bath and sonicated (Bransonic Model 2510) to disperse the lipid film. Samples were then topped off again with perfluorpropane gas and mechanically agitated for 45s using a VialMix® shaker. Samples were allowed to cool for 15min before use and were used within 30min of opening the vial to mitigate potential temporal effects on pMB properties.

pMBs were gently shaken for 10s and decanted for 2min before 500μl was extracted into a 3ml syringe. Using the differential centrifugation method[31], pMBs were separated from residual nanoparticles by centrifugation for 8min at 50G twice, washing with 10vol% propylene glycol, 10vol% glycerol and

80vol% PBS. For conversion US pulsing experiments, samples were diluted 6x in PBS and placed within 1ml eppendorf tubes. The samples were then situated in a water tank and sonicated with 1MHz ultrasound (Vevo® SoniGene™, FUJIFILM VisualSonics, Inc.) using the 10W setting (2W/cm^2 intensity, 50% duty cycle, 2s long pulses). The exposures consisted of the application of 0, 1, 3 or 10 pulses (separated by 5s). These settings were selected based on pilot experiments that were found to progressively decrease pMB concentrations with each pulse and are similar to those previously used by others in microbubble drug delivery[32]. However, conversion was also observed with lower duty cycles (10% and 20%) to generate spherical nanoparticles (Supplementary Figure 15).

pMB concentration was determined using a Coulter Counter Multisizer Z3 (Beckman Coulter Inc.), in which pMB samples were diluted in Isoton-II electrolyte solution (Beckman Coulter Inc.) to obtain a count within 100 000 – 300 000 in a 50μl volumetric sample. A background count of buffer was taken and subtracted from the final count. Dilution was accounted for in calculating the pMB concentration. The number and size distribution were measured using a 30μm aperture which detected pMBs with diameters in the range 0.8 - 18μm.

pNP size distribution and concentration was measured using a NanoSight LM10 and Nanoparticle Tracking Analysis Software (Malvern Instruments Ltd, Malvern, UK). Pulsed samples were centrifuged using a bench top ultracentrifuge after conversion US pulses were applied and 200μl of the infranant was removed from the bottom of the sample, collecting only pNPs as the remaining pMBs formed a cake on the top. Samples were then diluted with PBS 2x before measuring the size distribution and concentration.

pMB acoustic characterization and ultrasound imaging in solution

The acoustic attenuation spectrum of pMBs was measured using a narrowband pulse-echo substitution method similar to that used by Helfield et al[33]. Using two transducers (Model #595396, 5MHz, 76mm focus, 12.7mm diameter, Olympus NDT Canada Inc.; Model #IS2002HR, 20MHz, 38mm focus, 6.35mm diameter, Valpey-Fisher), the attenuation was measured in the frequency range between 1.5 - 27.5MHz in 0.5MHz increments. US pulses were generated by an arbitrary waveform generator (model WW2572A, Tabor Electronics Ltd., Tel Hanan, Israel) and amplified (model A-150; ENI, Rochester, NY) before reaching each transducer; voltages were calibrated for each transducer to deliver 25kPa peak negative pressure at its geometric focus for each frequency. An aluminium rod was placed at each transducer's focus to serve as a reflector to generate echoes that were detected by the same transducer. Echoes were then amplified (model AU1579; Miteq, Hauppauge, NY) and bandpass filtered before being digitized (400MHz sampling frequency; Agilent Technologies Inc., Palo Alto, CA) for post-process analysis. Acquisitions occurred prior to and after introducing pMBs (1:15000 contrast agent to saline dilution ratio) in a chamber with an acoustically transparent window between the transducer and

aluminium reflector. The attenuation per unit length was calculated at each frequency by comparing the echo amplitudes and knowing the distance through which US interacted with the pMBs.

Linear and non-linear US imaging was performed in a tissue-mimicking flow phantom similar to that described by Helfield et al.[33] and imaged using a Phillips iU22 clinical scanner with a L9-3 probe (3-9MHz) (Phillips Medical Systems, Seattle, WA) operating in B-mode for linear imaging and contrast mode for non-linear imaging. The tissue-mimicking phantom was composed of a 2% agar and 3% graphite medium, the latter acting as an acoustic scatterer, with an acoustic attenuation of 0.3 dB/mm/MHz as reported by Burlew et al.[34] A wall-less vessel was created by placing a 6.3mm diameter rod within the phantom prior to casting; after the gel solidified the rod was removed. pMBs were diluted with gas-equilibrated saline (0.9% (w/v) NaCl) at a ratio of 1:5000 in a reservoir and mixed with a magnetic stirrer to ensure a representative population of agent was being used. After 30s of mixing, the diluted agent was allowed to flow through the phantom using a gravity feed approach. The flow rate was maintained around 8-9mm/s in order to minimize decorrelation effects in contrast mode. The agent required ~ 1min to reach the imaging plane (with the vessel located 4.5cm below the surface) from the reservoir. US images were captured 2min and 20s post agent dilution.

pMB and pNP microscopy

pMBs were diluted 50x for imaging with confocal microscopy (Olympus FluoView FV1000) using a 633nm laser and 40x water objective lens. pNPs were imaged with transmission electron microscopy (TEM) (Hitachi H-7000 electron microscope) with an acceleration voltage of 75kV. Samples that were pulsed 10 or 20 times and were prepared for TEM by applying 10μl of pNPs to a glow-discharged 200-mesh copper-coated grid, washed once with deionized water and stained with 2% (w/v) uranyl acetate.

Vacuum pressure experiments were performed on pNP samples after the pMBs had 10 conversion US pulses applied, using conditions similar to those described by Huang et al.[35] The pNP samples were transferred to a 2ml glass vial with a screw cap and syringe seal closure. A 5ml syringe with a 25G needle was introduced through the seal and the plunger of the syringe was withdrawn to obtain a pressure of 0.5atm, determined from the vapour phase volume in the vial and the syringe according to Boyle's law. The pressure was maintained for 3 minutes and then the samples were imaged using TEM.

Optical characterization

To measure the UV/Visible absorption spectra of pMBs and pNPs, samples were diluted 8x in PBS or 50vol% fetal bovine serum (FBS) and measured using a Cary 50 UV-visible spectrophotometer (Agilent, Mississauga, ON), scanning from 300nm - 900nm. Circular dichroism spectra were determined

in PBS for pMBs and pNPs using a J-815 Circular Dichroism Spectrometer (JASCO Inc.) scanning from 300nm – 900nm. The fluorescence spectra of 8x diluted pMBs and pNPs samples were measured in PBS using a Fluoromax-4 spectrofluorometer (Horiba Jobin Yvon, NJ). Fluorescence emission was collected 700nm – 900nm using an excitation of 520nm and 5nm slit widths. Measurements of BChl-lipid monomeric samples were obtained by adding Triton X-100 to pNPs to disrupt the nanoparticle structure and BChl ordered aggregates (final detergent concentration: 1vol%).

pNP field flow-field fractionation (F4)

100µl of a 1mg/ml sample of pNPs or 100µl of PBS was injected into the channel of the F4 instrument (DualTec Eclipse Separation System) (Wyatt Technology). The "short channel" (145mm length) (Wyatt Technology) was used, equipped with the W250µm spacer (Wyatt Technology) and a 5kDa cellulose membrane (Wyatt Technology). Throughout the procedure the detector flow remained constant at 1ml/min. Upon injection, the sample was focused with a focus flow-rate of 1ml/min over 5min after which the focusing stopped. A constant cross flow of 0.1ml/min was then applied over 35min. The cross-flow was then removed for the remaining 30min of elution. UV absorbance was tracked at 380nm using the 1200 series variable wavelength detector (Agilent). Static light scattering at 19 angles was tracked using the DAWN HELEOS-II detector (Wyatt Technology).

The light scattering data was analysed using ASTRA version 6.1.2.84 (Wyatt Technologies) to determine RMS^2 of the pNPs eluted at a given time. The RMS^2 was then converted to radius (R) using the following equation: $RMS^2=3/5\ R^2$, assuming the pNPs are a solid sphere. The Zimm model was applied to the scattering data of the first peak (first order fit), and the Berry model to the second peak (second order fit).

pMB and pNP stability measurements

pMB stability in solution was measured over time using the Coulter Counter Multisizer Z3 as previously described. Samples were measured immediately after opening the pMB sample vial, 0.5hr and 1hr. pMBs were converted into pNPs in PBS and pNP stability was measured in solution using the NanoSight LM10 up to 22 days post-formation.

pNP stability in FBS was determined by absorbance of the 824nm aggregation peak. pMBs were diluted in fetal bovine serum to a final serum concentration of 80vol%. Samples were then subjected to 10 conversion US pulses to generate pNPs in serum. Absorbance was measured using a plate reader at 824nm (BChl J-aggregation peak) and 750nm (monomer BChl peak) over time up to 12hrs.

pMB and pNP imaging in a gel phantom

pMBs and pNPs were immobilized in a polyacrylamide hydrogel phantom that was prepared using a similar method described by Ng et al.[25]. Briefly, 59mL of ddH_2O, 30mL of 30% (w/v) 19:1 acrylamide (Biorad, Mississauga, ON) and 10mL of 1M Tris buffer (pH 8) were degassed for 20min. Ammonium persulfate (APS; 10% w/v) and N,N,N′ ,N′ -tetramethylethylenediamine (TEMED) were added to the monomer mixture to a final concentration of 0.84% and 0.2%, respectively, mixed, poured into a gel mold with a comb and allowed to polymerize for 1hr. After 1hr, the comb was removed and the same mixture with the pMBs or pNPs (5x diluted) in place of a volume of ddH_2O was poured into the 2mm x 2mm x 20mm empty cavities and allowed to polymerize.

US and photoacoustic imaging were performed with a commercial photoacoustic imaging system (Vevo LAZR: FUJIFILM VisualSonics, Inc.), operating with a 21MHz transducer in both US and photoacoustic modes. US and photoacoustic images were obtained with 25dB and 40dB gains, respectively. Photoacoustic spectra were obtained from 680nm to 900nm with 2nm steps. Fluorescence images were obtained using a whole-body small animal imager (CRi Maestro: Caliper Life Science Inc.) under green-light excitation (503nm - 548nm), 560nm long pass detection, an integration time of 700ms and then spectrally unmixed. Comparisons between 0 pulses and pulsed samples were made using the two-sample homoscedastic Student's t-Test, with the level of significance was set at $p < 0.05$.

pMB to pNP in vivo imaging and blood collection

Animal experiments were conducted in compliance with institutional animal care approval (University Health Network). The model was generated by subcutaneous inoculation of 2×10^6 KB cells in the right flank of 20g female athymic nude mice. Experiments were performed when tumours reached a surface diameter of 5-7mm. Mice were anesthetized with 2% (v/v) isoflurane inhalation to insert a 26 gauge-indwelling catheter into the tail vein. Mice were then injected with 100mg/kg of ketamine and 10mg/kg of xylazine via intraperitoneal injection and removed from isoflurane inhalation.

pMB *in vivo* stability was determined via the *in vivo* circulation time as observed by US imaging by injecting a 150µl bolus of (8.4±0.4) x 10^7 pMB/ml followed by a 100µl saline flush. The tumour was then imaged using the Vevo 2100 ultrasound system (FUJIFILM VisualSonics, Inc.) and the MS250 probe operating at a frequency of 13-24MHz. Region of interest analysis was conducted by selecting a region inside of the tumour, and normalizing it to the maximum US signal determined after injecting the pMBs. Trendlines were plotted using a 10 period moving average using Microsoft Excel.

pMB to pNP conversion *in vivo* experiments were also performed on female athymic nude mice bearing subcutaneous KB tumours in the right flank. For "no conversion US applied" control animals, mice were injected with a 150µl bolus of (8.4±0.4) x 10^7 pMB/ml followed by a 100µl saline flush. Mice were monitored with photoacoustic imaging over time (assessed at 5min and 15min post-injection and

then at 15min intervals up to 2hrs) using a 21MHz transducer and at wavelengths of 824nm and 850nm for photoacoustics.

For "conversion US applied" animals, mice were harnessed to a custom animal holder shown in Supplementary Figure 16, and immersed in a 35°C heated water tank. Conversion US and imaging US transducers were aligned to both irradiate the tumour region with conversion US and simultaneously image the pMB influx and externally triggered destruction using US imaging as shown in Supplementary Figure 16. The conversion US transducer was aligned to a distance of 1cm from the surface of the centre of the tumour using a custom-made detachable alignment tool cap for the conversion US transducer (Supplementary Figure 17). After removal of the alignment tool and repositioning of the conversion US transducer, the imaging US transducer (Vevo 2100, 13-24MHz functioning in B-mode and contrast mode) was placed over the tumour in order to image the pMB influx and destruction. Mice were injected with a 150µl bolus of (8.4±0.4) x 10^7 pMB/ml followed by a 100µl saline flush. 20s after pMB injection, circulation of pMB was visible via US imaging, and the tumour was then sonicated with 60s of 10W ($2W/cm^2$) and 50% duty cycle conversion US. Mice were then removed from the heated water bath and placed in the Vevo LAZR system for photoacoustic imaging. Photoacoustic imaging was performed at 5min and 15min post-injection and then in 15min intervals up to 2hrs. Photoacoustic images were processed by subtracting the images acquired at 850nm from that at 824nm to remove any background signal. Region of interest (ROI) analysis was performed using software provided by the Vevo LAZR by selecting a region in the tumour, which calculated the average photoacoustic intensity in that region. ROIs were selected on images acquired at 824nm and were subtracted from the average intensity photoacoustic value at 850nm in the same region to account for background signal. These values were then normalized to the maximum photoacoustic signal over time. For ROI analysis of US images, a region inside the tumour was selected on the contrast mode images, providing the contrast mean power. These values were then expressed as a percentage of the maximum contrast mean power. Trendlines were plotted using a 10 period moving average using Microsoft Excel.

To assess the fluorescence spectra of pMBs after circulation *in vivo*, mice were injected with a 150µl bolus of (8.4±0.4) x 10^7 pMB/ml followed by a 100µl saline flush. After 5 or 15min post-injection, 500µl of blood was collected via intracardiac puncture using a syringe rinsed with 5% heparin saline. Mice were sacrificed immediately after blood collection. Whole blood was imaged in eppendorf tubes by fluorescence imaging (CRi Maestro: Caliper Life Science Inc.) under green-light excitation (503nm - 548nm), 560nm long pass detection, an integration time of 5000ms and then spectrally unmixed.

References:

1. Motornov M, Zhou J, Pita M, Gopishetty V, Tokarev I, Katz E, *et al.* "Chemical transformers" from nanoparticle ensembles operated with logic. *Nano letters* 2008, **8**(9)**:** 2993-2997.

2. Ng KK, Lovell JF, Vedadi A, Hajian T, Zheng G. Self-assembled porphyrin nanodiscs with structure-dependent activation for phototherapy and photodiagnostic applications. *ACS nano* 2013, **7**(4)**:** 3484-3490.

3. Skirtach AG, Antipov AA, Shchukin DG, Sukhorukov GB. Remote activation of capsules containing Ag nanoparticles and IR dye by laser light. *Langmuir : the ACS journal of surfaces and colloids* 2004, **20**(17)**:** 6988-6992.

4. Melancon MP, Zhou M, Li C. Cancer theranostics with near-infrared light-activatable multimodal nanoparticles. *Accounts of chemical research* 2011, **44**(10)**:** 947-956.

5. Kripfgans OD, Fowlkes JB, Miller DL, Eldevik OP, Carson PL. Acoustic droplet vaporization for therapeutic and diagnostic applications. *Ultrasound in medicine & biology* 2000, **26**(7)**:** 1177-1189.

6. Rapoport N, Nam KH, Gupta R, Gao Z, Mohan P, Payne A, *et al.* Ultrasound-mediated tumor imaging and nanotherapy using drug loaded, block copolymer stabilized perfluorocarbon nanoemulsions. *Journal of controlled release : official journal of the Controlled Release Society* 2011, **153**(1)**:** 4-15.

7. Wei K, Jayaweera AR, Firoozan S, Linka A, Skyba DM, Kaul S. Quantification of myocardial blood flow with ultrasound-induced destruction of microbubbles administered as a constant venous infusion. *Circulation* 1998, **97**(5)**:** 473-483.

8. Ferrara K, Pollard R, Borden M. Ultrasound microbubble contrast agents: fundamentals and application to gene and drug delivery. *Annual review of biomedical engineering* 2007, **9:** 415-447.

9. Chomas JE, Dayton P, Allen J, Morgan K, Ferrara KW. Mechanisms of contrast agent destruction. *IEEE transactions on ultrasonics, ferroelectrics, and frequency control* 2001, **48**(1)**:** 232-248.

10. Sboros V, Moran CM, Pye SD, McDicken WN. Contrast agent stability: a continuous B-mode imaging approach. *Ultrasound in medicine & biology* 2001, **27**(10)**:** 1367-1377.

11. Huynh E, Zheng G. Engineering multifunctional nanoparticles: all-in-one versus one-for-all. *Wiley interdisciplinary reviews Nanomedicine and nanobiotechnology* 2013, **5**(3)**:** 250-265.

12. Huynh E, Jin CS, Wilson BC, Zheng G. Aggregate Enhanced Trimodal Porphyrin Shell Microbubbles for Ultrasound, Photoacoustic, and Fluorescence Imaging. *Bioconjugate chemistry* 2014.

13. Huynh E, Lovell JF, Helfield BL, Jeon M, Kim C, Goertz DE, *et al.* Porphyrin shell microbubbles with intrinsic ultrasound and photoacoustic properties. *Journal of the American Chemical Society* 2012, **134**(40)**:** 16464-16467.

14. Liu Z, Lammers T, Ehling J, Fokong S, Bornemann J, Kiessling F, *et al.* Iron oxide nanoparticle-containing microbubble composites as contrast agents for MR and ultrasound dual-modality imaging. *Biomaterials* 2011, **32**(26)**:** 6155-6163.

15. Kabalnov A, Bradley J, Flaim S, Klein D, Pelura T, Peters B, *et al.* Dissolution of multicomponent microbubbles in the bloodstream: 2. Experiment. *Ultrasound in medicine & biology* 1998, **24**(5)**:** 751-760.

16. Luan Y, Lajoinie G, Gelderblom E, Skachkov I, van der Steen AF, Vos HJ, *et al.* Lipid shedding from single oscillating microbubbles. *Ultrasound in medicine & biology* 2014, **40**(8)**:** 1834-1846.

17. Cox DJ, Thomas JL. Rapid shrinkage of lipid-coated bubbles in pulsed ultrasound. *Ultrasound in medicine & biology* 2013, **39**(3)**:** 466-474.

18. Sengupta S, Wurthner F. Chlorophyll J-aggregates: from bioinspired dye stacks to nanotubes, liquid crystals, and biosupramolecular electronics. *Accounts of chemical research* 2013, **46**(11)**:** 2498-2512.

19. Wang LV, Hu S. Photoacoustic tomography: in vivo imaging from organelles to organs. *Science* 2012, **335**(6075)**:** 1458-1462.

20. Kopechek JA, Haworth KJ, Radhakrishnan K, Huang SL, Klegerman ME, McPherson DD, *et al.* The impact of bubbles on measurement of drug release from echogenic liposomes. *Ultrasonics sonochemistry* 2013, **20**(4)**:** 1121-1130.

21. Lovell JF, Jin CS, Huynh E, Jin H, Kim C, Rubinstein JL, *et al.* Porphysome nanovesicles generated by porphyrin bilayers for use as multimodal biophotonic contrast agents. *Nature materials* 2011, **10**(4)**:** 324-332.

22. Liu TW, Macdonald TD, Jin CS, Gold JM, Bristow RG, Wilson BC, *et al.* Inherently multimodal nanoparticle-driven tracking and real-time delineation of orthotopic prostate tumors and micrometastases. *ACS nano* 2013, **7**(5)**:** 4221-4232.

23. Liu TW, MacDonald TD, Shi J, Wilson BC, Zheng G. Intrinsically copper-64-labeled organic nanoparticles as radiotracers. *Angewandte Chemie* 2012, **51**(52)**:** 13128-13131.

24. MacDonald TD, Liu, T. W, Zheng, G. . An MRI-Sensitive, Non-Photobleachable Porphysome Photothermal Agent. *Angewandte Chemie* 2014.

25. Ng KK, Shakiba M, Huynh E, Weersink RA, Roxin A, Wilson BC, *et al.* Stimuli-responsive photoacoustic nanoswitch for in vivo sensing applications. *ACS nano* 2014, **8**(8)**:** 8363-8373.

26. Jin CS, Cui L, Wang F, Chen J, Zheng G. Targeting-Triggered Porphysome Nanostructure Disruption for Activatable Photodynamic Therapy. *Advanced healthcare materials* 2014.

27. Jin CS, Lovell JF, Chen J, Zheng G. Ablation of hypoxic tumors with dose-equivalent photothermal, but not photodynamic, therapy using a nanostructured porphyrin assembly. *ACS nano* 2013, **7**(3)**:** 2541-2550.

28. Prabhakar U, Maeda H, Jain RK, Sevick-Muraca EM, Zamboni W, Farokhzad OC, *et al.* Challenges and key considerations of the enhanced permeability and retention effect for nanomedicine drug delivery in oncology. *Cancer research* 2013, **73**(8)**:** 2412-2417.

29. Wang YH, Chen SP, Liao AH, Yang YC, Lee CR, Wu CH, *et al.* Synergistic delivery of gold nanorods using multifunctional microbubbles for enhanced plasmonic photothermal therapy. *Scientific reports* 2014, **4:** 5685.

30. Berg K, Selbo PK, Weyergang A, Dietze A, Prasmickaite L, Bonsted A, *et al.* Porphyrin-related photosensitizers for cancer imaging and therapeutic applications. *Journal of microscopy* 2005, **218**(Pt 2)**:** 133-147.

31. Feshitan JA, Chen CC, Kwan JJ, Borden MA. Microbubble size isolation by differential centrifugation. *Journal of colloid and interface science* 2009, **329**(2)**:** 316-324.

32. Li P, Zheng Y, Ran H, Tan J, Lin Y, Zhang Q, *et al.* Ultrasound triggered drug release from 10-hydroxycamptothecin-loaded phospholipid microbubbles for targeted tumor therapy in mice. *Journal of controlled release : official journal of the Controlled Release Society* 2012, **162**(2)**:** 349-354.

33. Helfield BL, Huo X, Williams R, Goertz DE. The effect of preactivation vial temperature on the acoustic properties of Definity. *Ultrasound in medicine & biology* 2012, **38**(7)**:** 1298-1305.

34. Burlew MM, Madsen EL, Zagzebski JA, Banjavic RA, Sum SW. A new ultrasound tissue-equivalent material. *Radiology* 1980, **134**(2)**:** 517-520.

35. Huang SL, Hamilton AJ, Pozharski E, Nagaraj A, Klegerman ME, McPherson DD, *et al.* Physical correlates of the ultrasonic reflectivity of lipid dispersions suitable as diagnostic contrast agents. *Ultrasound in medicine & biology* 2002, **28**(3)**:** 339-348.

Acknowledgements:

The authors thank Aron Roxin for providing the BChl-lipid, Patrick McVeigh for technical assistance with the NanoSight LM10, Maria Balassu for technical assistance with the animal study and Danielle M. Charron for help with the electron microscopy. We also thank Ren-Ki Li for usage of his Vevo® SoniGene™ instrument. This work was supported by the Canadian Institutes of Health Research (CIHR) Frederick Banting and Charles Best Canada Graduate Scholarship, the Emerging Team Grant on Regenerative Medicine and Nanomedicine co-funded by the CIHR and the Canadian Space Agency, the Natural Sciences and Engineering Research Council of Canada, the Ontario Institute for Cancer Research, the International Collaborative R&D Project of the Ministry of Knowledge Economy, South Korea, the Joey and Toby Tanenbaum/Brazilian Ball Chair in Prostate Cancer Research, the Canada Foundation for Innovation, and the Princess Margaret Cancer Foundation.

Additional information:

Supplementary information accompanies this paper at www.nature.com/naturenanotechnology. Reprints and permission information is available online at http://npg.nature.com/reprintsandpermissions/. Correspondence and requests for materials should be addressed to G.Z.

Author contributions:

E.H. and G.Z. conceived the idea, interpreted the data and wrote the manuscript. E. H., D.E.G. and G.Z. designed the experiments. E.H. carried out size characterization, light microscopy, optical characterization and imaging studies. B.Y.C.L., B.L.H. and E.H. performed the acoustic characterization. M.S. and E.H. carried out electron microscopy. E.H. and C.S.J. carried out animal imaging experiments. J.G. and E.R.M carried out flow field-flow fractionation. E.H., D.E.G., B.C.W. and G.Z. edited the manuscript.

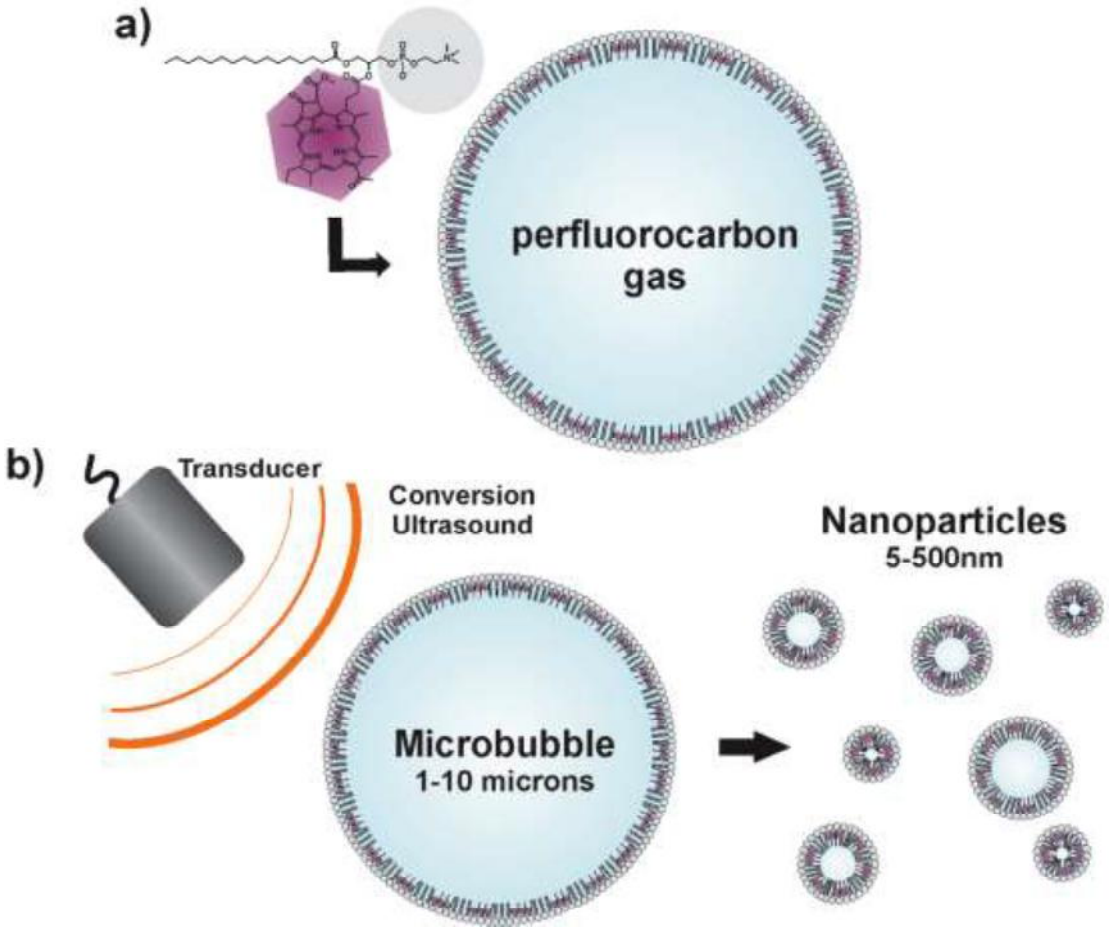

Figure 1. Schematics of porphyrin microbubbles (pMBs) and their micro-to-nano conversion. a) pMBs consist of a BChllipid shell encapsulating perfluoropropane gas. b) Conversion of pMBs to porphyrin nanoparticles (pNPs) via sonication with low frequency, high duty cycle ultrasound (conversion ultrasound).

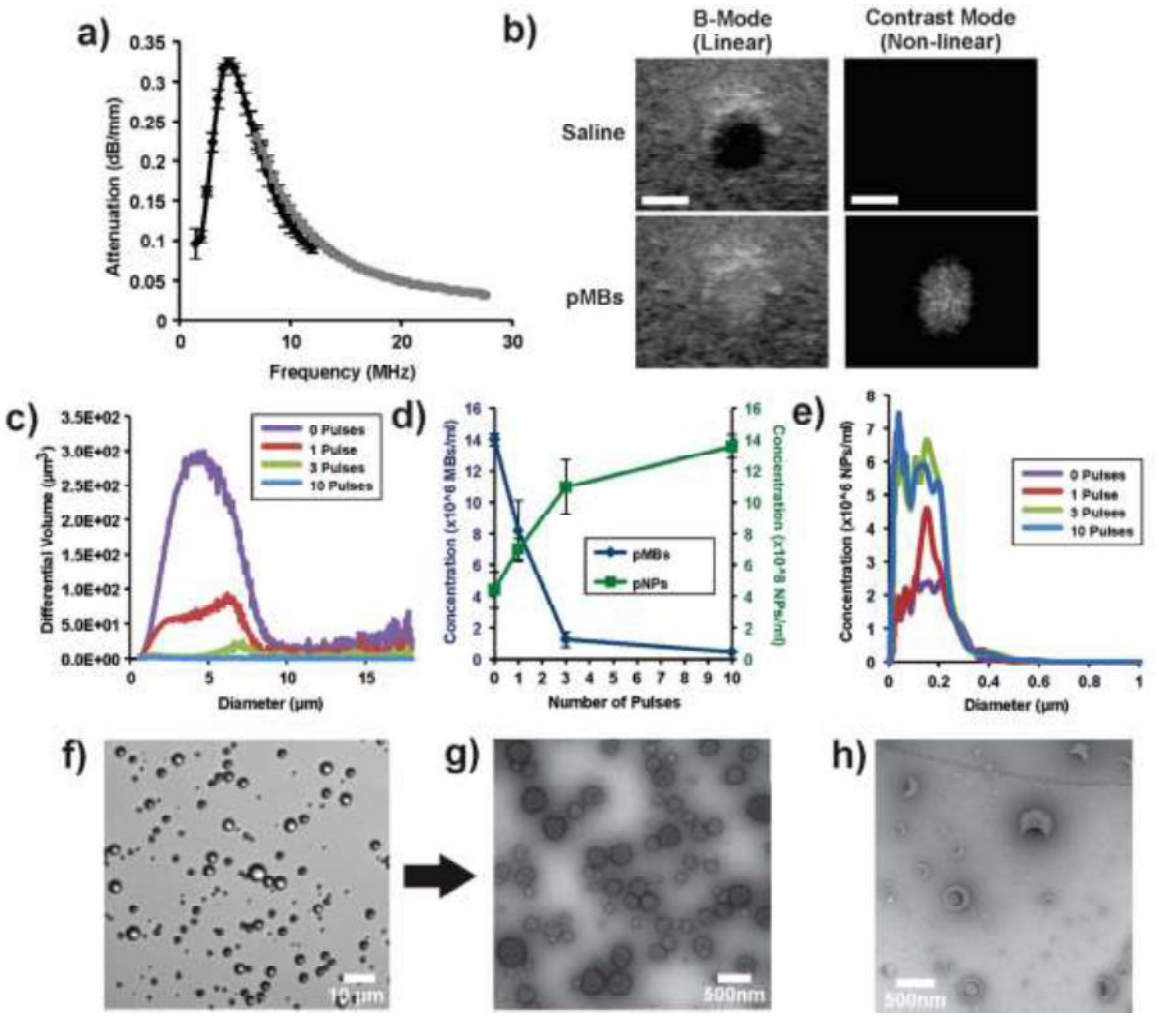

Figure 2. Characterization of the conversion of pMBs to pNPs. a) Acoustic attenuation measurement of pMBs with a resonance frequency of 4.5MHz using two transducers (black line: transducer 1: 1.5 – 12MHz; grey line: transducer 2: 7 – 27.5MHz). Mean ± 1 S.D. with n=3. pMBs possess a resonance attenuation peak at 4.5MHz. b) Linear and non-linear US properties of pMBs. A tissue mimicking flow phantom composed of agar and graphite was used with a wall-less vessel in which pMBs or saline were allowed to flow through and imaged with a clinical US scanner. B-mode (linear) and contrast mode (non-linear) US imaging of saline (top) and pMBs (bottom). The phantom produced linear backscatter shown in the B-mode image, similar to tissue, but did not possess non-linear properties, shown by a lack of contrast in the contrast mode image. pMBs generate both linear and non-linear US signals. 5mm scale bar shown. c) Size distribution of pMBs prior to and after application of conversion US pulses according to volume distribution. After interaction with conversion US pulses, the pMB volume population decreased. d) Concentration of pMBs and pNPs before and after application of conversion US pulses. pMB concentration decreased and pNP concentration increased with increased number of conversion US pulses. Mean ± 1 S.D. with n=3. e) Size distribution of pNPs after conversion US pulses were applied. f) Light microscopy image of pMBs. g) Transmission electron microscopy (TEM) image of pNPs formed from pMBs after 10 US pulses. h) TEM image of liposome-like structures formed from pNPs after placing pNPs in a vacuum.

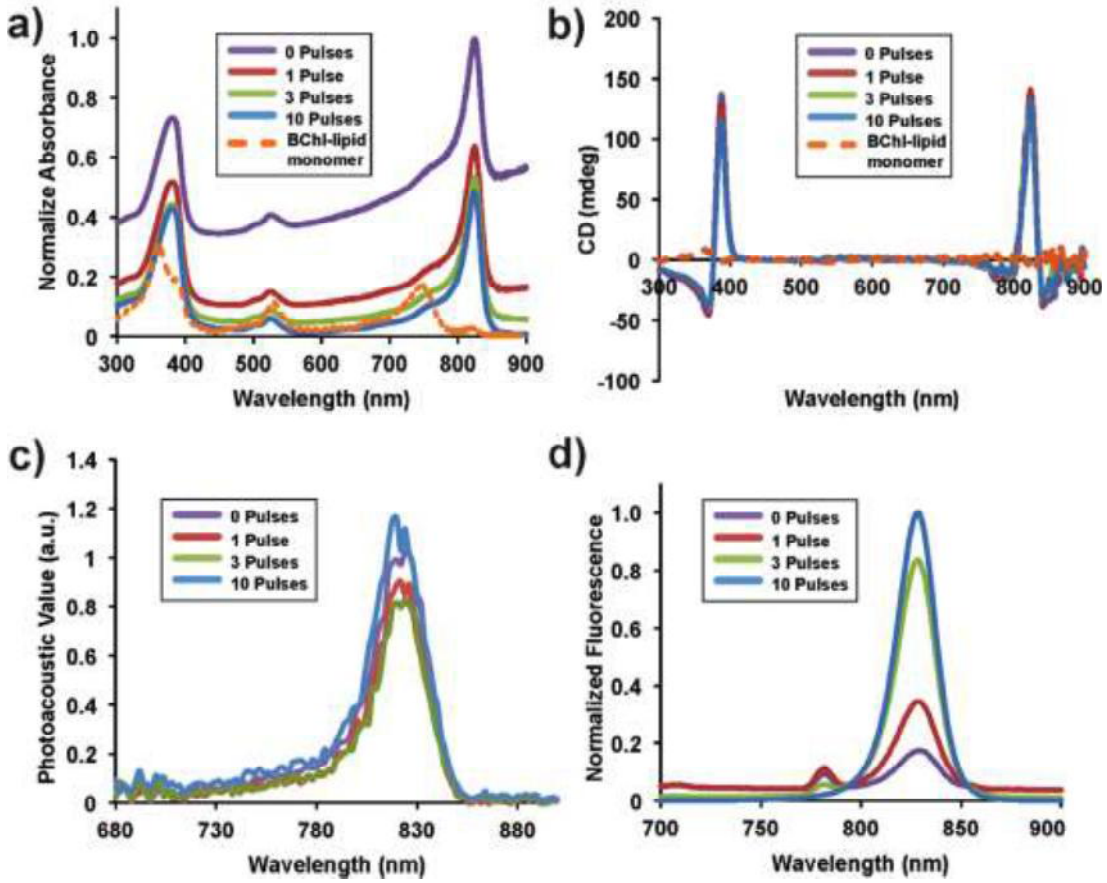

Figure 3. Optical spectra of pMBs and resulting pNPs after interaction with conversion US. a) Absorption spectra and b) circular dichroism spectra of pMBs after several conversion US pulses compared with BChl-lipid in its monomeric form. BChl-lipid monomer samples were pNPs disrupted using 1vol% Triton-X100. pNPs maintain the ordered aggregation peak associated with pMBs after conversion. c) Photoacoustic and d) fluorescence spectra of pMBs before and after applying US. pNPs maintain the fluorescence emission and photoacoustic peaks associated with pMBs.

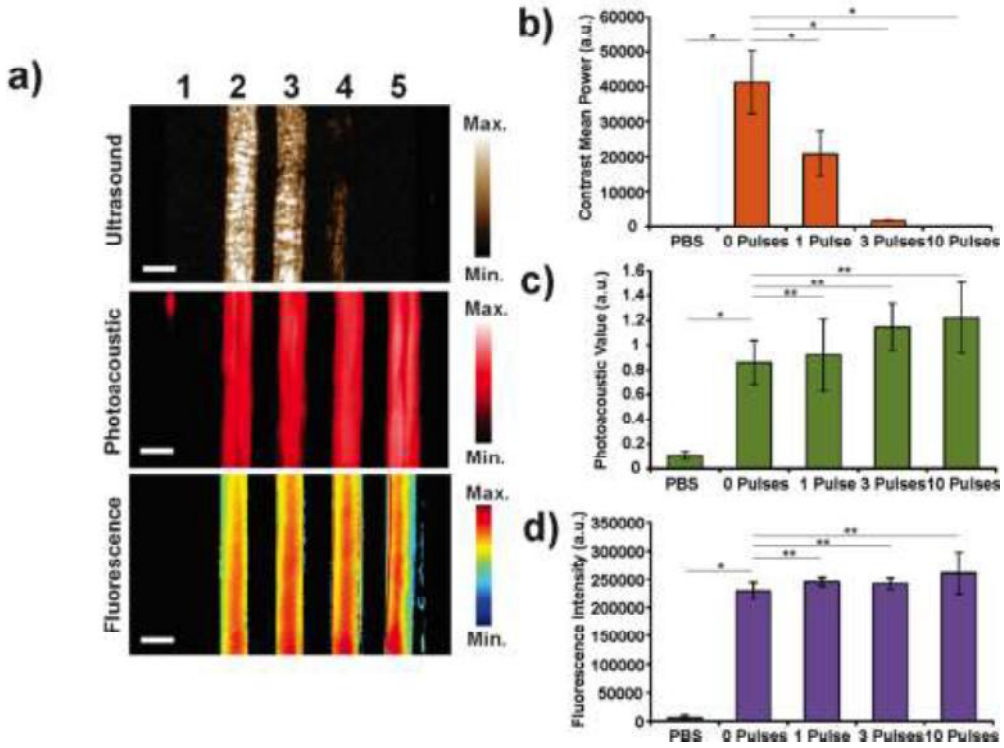

Figure 4. Multimodal imaging of pMBs and resulting pNPs upon US induced conversion. a) pMBs and pNPs embedded in an acrylamide gel phantom were imaged using US (13-24MHz transducer in contrast mode), photoacoustic (21MHz transducer, 824nm) and fluorescence (green exc. 503 nm - 548 nm; 560nm long pass detection). Samples: 1) phosphate buffered saline (PBS), 2) pMBs without applying US pulses – 0 pulses, 3) 1 pulse, 4) 3 pulses, 5) 10 pulses. 2mm scale bar shown. b-d) Quantified signals from US (b), photoacoustic (c), and fluorescence imaging (d). Data are expressed as mean values (n=3) ± 1 standard deviation; *p < 0.05; **p > 0.05. pMBs generate US, photoacoustic and fluorescence imaging contrast. After conversion to pNPs, they generate only photoacoustic and florescence contrast.

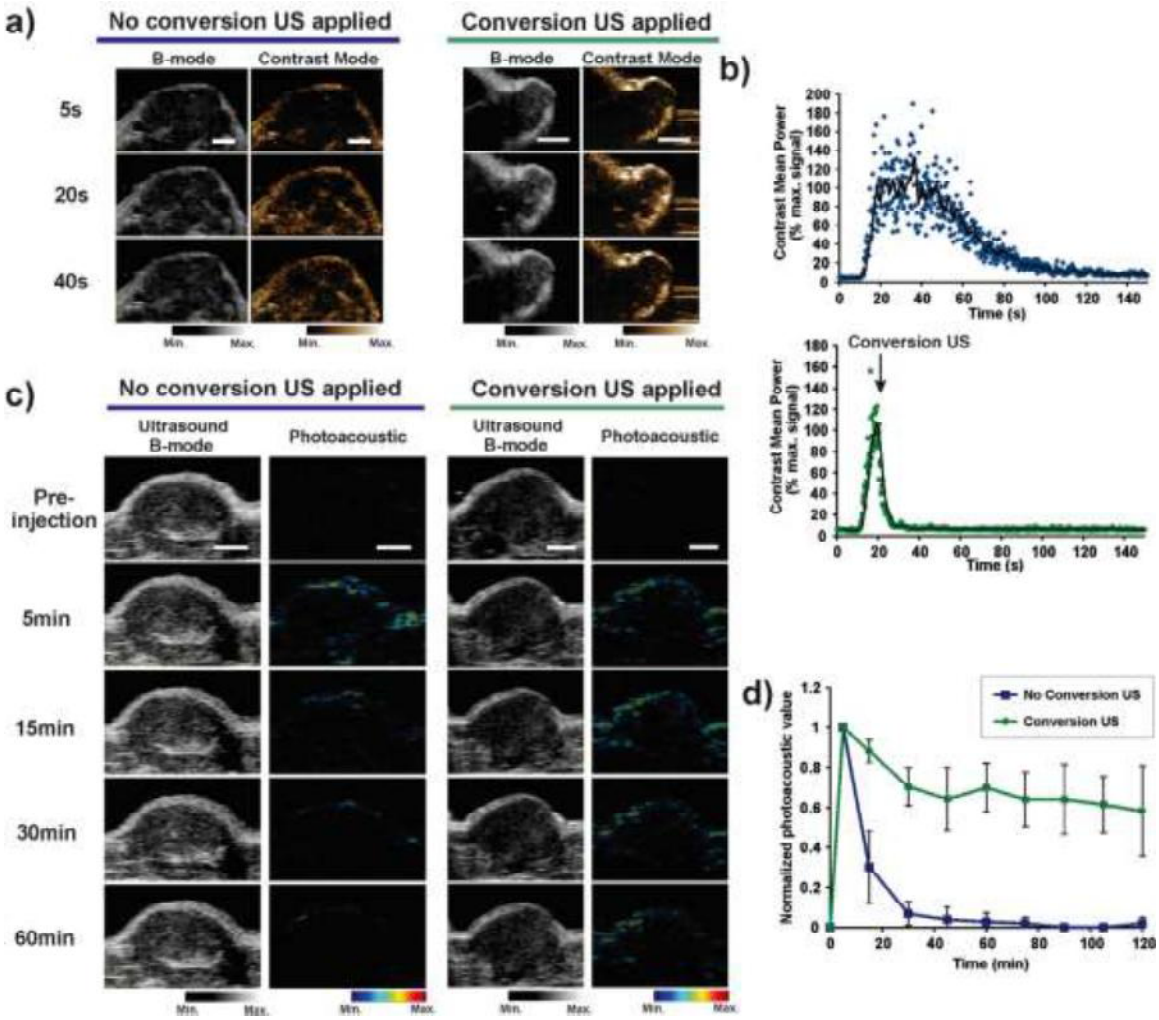

Figure 5. Conversion of pMBs to pNPs *in vivo* in mice. a) pMBs were intravenously administered into KB xenograft bearing mice and a cross section of the tumor was imaged using high frequency US. After injection, the pMBs circulated into the tumor, reaching a peak in circulation at 20s and could continuously be observed in circulation beyond 40s. 2mm scale bar shown. When conversion US was applied after the 20s time point, a decrease in contrast mode US signal was observed, for example at 40s. 3mm scale bar shown. b) Region of interest analysis of the contrast mean power expressed as a percentage of the mean maximum signal in the tumor without conversion US applied (top) and with conversion US applied after the 20s time point (bottom). Black line indicates a 10 period moving average trend line. c) Conversion of pMBs to pNPs in tumor xenografts enabled the retention of pNPs in the tumor confirmed by photoacoustic imaging. Photoacoustic images of the tumor xenograft without or with conversion US applied over time. 2mm scale bars shown. d) Normalized photoacoustic signal over time in the tumor in which conversion US was not applied (blue) or was applied (green). Photoacoustic values normalized to the peak photoacoustic value. Mean ± 1 S.D. with n=3. Only in tumors in which conversion US was applied does the pNP remain at the tumor site, indicating successful delivery to the tumor.